Influence of hexadecapole and hexacontatetrapole deformations and associated orientations on the synthesis of superheavy nuclei

Diksha[†] Harshit Sharma[‡] Manoj K. Sharma[§]

Department of Physics and Materials Science, Thapar Institute of Engineering & Technology, Patiala- 147004, Punjab, India

Abstract: This study examines the impact of higher-order deformations up to hexacontatetrapole (β_6) deformation on the synthesis of superheavy nuclei (SHN) through heavy-ion induced fusion reactions. The main objective of the study is to examine the impact of modified nuclear shapes that result from the collective influence of deformations (up to β_6) on the barrier characteristics V_B and R_B and overall dynamics of nuclear reactions leading to the synthesis of SHN. The analysis takes into account both spherical+deformed and deformed+deformed projectile-target (P-T) combinations that lead to the synthesis of SHN. Furthermore, the analysis examines the influence of the sign (±) and magnitude of β_6 on the barrier characteristics and overall reaction dynamics. This analysis is performed by utilizing ^{48}Ca, ^{36}S, and ^{48}Ti induced reactions with β_6-deformed actinide targets. The compact and elongated orientations, influenced by the sign and magnitude of β_2, β_4, and β_6 deformations, respectively, introduce further modifications in the reaction dynamics.The calculated capture cross-sections ($\sigma_{\rm cap}$) result in better agreement with the experimental data for the case which incorporates β_6 along with β_2 and β_4 deformations than for the $\beta_2\beta_4$ deformations due to modified barrier characteristics, particularly at near-barrier energies. The findings underscore the importance and impact of incorporating deformations (up to β_6) and their corresponding orientations to achieve a thorough understanding of the dynamics of heavy-ion induced reactions pertaining to the superheavy mass region.

Keywords: nuclear deformation, nuclear fusion, superheavy nuclei, nuclear reaction

DOI: 10.1088/1674-1137/ae1c2a **CSTR:** 32044.14.ChinesePhysicsC.50034101

I. INTRODUCTION

Investigation into the characteristics and synthesis of superheavy nuclei (SHN) has emerged as a prominent area of research in nuclear physics over the past few decades. The exploration of these elements offers a distinctive opportunity to probe the limits of the periodic table and explore the "island of stability," which is characterized by magic numbers Z=120,126 and N=184 [1−6]. Numerous theoretical and experimental studies have offered valuable insights into the synthesis of SHN via heavy-ion-induced reactions. These studies revealed several factors that influence the dynamics of these reactions within the low-energy domain [7−15]. Firstly, the synthesis of SHN requires the interacting nuclei to overcome the repulsive Coulomb barrier in order to create a compound nucleus through the exchange of nucleons and energy. The characteristics of this Coulomb barrier, *i.e.* the barrier height V_B and barrier position R_B, play a significant role, as they can hinder the formation of the new entity [16−19]. Studies examining the Coulomb barrier of such interactions suggest that numerous parameters such as mass, charge, energy, deformations, orientations, and angular momentum of the interacting nuclei can significantly influence the barrier height V_B and barrier position R_B of the Coulomb barrier [20−24]. Among these degrees of freedom, deformations of the interacting nuclei significantly influence both the barrier characteristics and the production of heavy and superheavy nuclei. Numerous investigations have been conducted to study the influence of quadrupole (β_2) deformations of interacting nuclei on the barrier characteristics and the capture cross-sections $\sigma_{\rm cap}$ [25−29]. To expand on the promising results of these investigations, we perform an in depth study of the influence of these higher-order deformations to explore adequate assessment of the reaction dynamics.

Recent studies have examined the effects of higher-order deformations on the synthesis of SHN, specifically focusing on octupole (β_3) and hexadecapole (β_4) deformations [25, 30−38]. To date, very few studies have analyzed and discussed the influence of hexacontatetrapole (β_6) and octacontatetrapole (β_8) deformations on the dy-

Received 15 August 2025; Accepted 6 November 2025; Accepted manuscript online 7 November 0202

[†] E-mail: dpathania1630@gmail.com

[‡] E-mail: hsharma.nph@gmail.com

[§] E-mail: msharma@thapar.edu

namics of heavy-ion induced reactions. Thus, an explicit analysis and comprehension concerning the influence of β_6 and β_8 deformations is lacking in literature. Furthermore, while the experimental evidence for the presence of β_6 in proton and alpha scattering from ^{238}U [39, 40] and ^{154}Sm [41] and on fusion reaction dynamics [37, 38, 42, 43] intrigues interest in the characteristics of β_6, similar insights regarding the β_8 deformation cannot be made due to the absence of experimental data. Therefore, investigating the influence and effect of the β_6 deformation on the synthesis of SHN via heavy-ion induced fusion reactions is of high interest.

In view of the deformations of the interacting nuclei, the elongated and compact configurations, determined by the extremes of the interaction barrier height (V_B) and the barrier position (R_B), significantly influence the reaction dynamics [17, 29, 36]. While the configuration containing the maximum V_B and minimal R_B values is termed a compact configuration, the configuration with the minimal V_B and the maximal R_B values is referred to as the elongated configuration. The influence of these configurations has been discussed and established in Refs. [17, 36, 44−47]. These configurations are significantly influenced by the incorporation of higher-order deformations. Therefore, this work analyzes the relevance of the β_6 deformation and associated orientations in reference to the barrier characteristics and capture cross-sections in the context of reactions leading to the synthesis of SHN.

For our analysis, we have considered the P-T combinations ^{48}Ca+^{248}Cm, ^{48}Ca+^{244}Pu, ^{48}Ca+^{238}U, ^{36}S+^{238}U , and ^{48}Ti+^{238}U leading to the formation of SHN ^{296}Lv, ^{292}Fl, ^{286}Cn, ^{274}Hs, and ^{286}Fl, respectively. The barrier characteristics of the modified nuclear shape due to the collective influence of the magnitude and sign (±) of the deformations (up to β_6) of the actinide target nuclei and their corresponding orientations are then used to determine the capture cross-sections ($\sigma_{\rm cap}$) for the considered P-T combinations using the ℓ-summed Wong formula [48, 49]. The static deformation parameters $\beta_2, \beta_4, \beta_6$ are referenced from the data table provided by Möller *et al.* [50]. The capture cross-sections ($\sigma_{\rm cap}$) are calculated for center of mass energies ($E_{\rm c.m.}$) that spread across the Coulomb barrier and are subsequently compared with the experimental data provided in Ref. [51]. Furthermore, we consider the P-T combination ^{48}Ca+^{246}Es with significant deformation magnitudes across the energy range of 180−220 MeV spanning the Coulomb barrier, to examine the effect of the magnitude and sign of the $\beta_2^{+}\beta_4^{\pm}\beta_6^{\pm}$ deformation. Thus, this work provides a thorough analysis of the modified barrier characteristics and reaction dynamics with the incorporation of β_2^{+}, $\beta_4^{\pm}$, and $\beta_6^{\pm}$ deformations. The findings advance our understanding of the dynamics associated with heavy-ion-induced reactions leading to the formation of SHN.

This manuscript is structured as follows: Section II provides a theoretical framework. Section III presents and discusses the results, emphasizing the role of the magnitude and signs (±) of hexacontatetrapole deformations (β_6) on the nuclear shape of deformed nuclei, the barrier characteristics, and the fusion reaction dynamics of actinides. Finally, Section IV presents a summary of the work done.

II. METHODOLOGY

A. Shape determination of the deformed nucleus

The shape of the deformed nuclei can be expressed through the radial vector $R_i(\alpha_i)$ equation in terms of the spherical harmonics $Y_{\lambda i}^{(0)}(\alpha_i)$ and the magnitude of the deformation $\beta_{\lambda i}$ [43, 50, 52, 53] as

$$\begin{aligned} R_i(\alpha_i) &= R_{0i}\left[1+\sum_{\lambda=2,3,4,6}\beta_{\lambda i}Y_{\lambda i}^{(0)}(\alpha_i)\right] \\ &= R_{0i}\left[1+\sum_{\lambda=2,3,4,6}\beta_{\lambda i}\sqrt{\frac{2\lambda+1}{4\pi}}P_\lambda(\cos\alpha_i)\right], \end{aligned} \quad (1)$$

where $i=1,2$ denotes the projectile and target of the interacting systems, respectively. The term R_{0i} signifies the radius of the corresponding spherical nuclei, defined by the equation $R_{0i}=1.28A_i^{1/3}-0.76+0.8A_i^{-1/3}$, measured in femtometers (fm) [54]. The variable λ indicates the order of deformation present in the nuclei, with values $\lambda=2,3,4,6$ corresponding to quadrupole, octupole, hexadecapole, and hexacontatetrapole deformations, respectively. The static deformation parameter $\beta_{\lambda i}$ is taken from the data table provided by Möller *et al.* [50]. The function $P_\lambda(\cos\alpha_i)$ represents the Legendre polynomial.

B. Total interaction potential

The colliding nuclei interact through an interaction potential (V_T), which comprises the sum of the attractive nuclear potential (V_N), repulsive Coulomb potential (V_C), and centrifugal potential (V_ℓ). The total interaction potential V_T is quantitatively expressed as follows:

$$\begin{aligned} V_T(R_i,A_i,\beta_{\lambda i},\theta_i) &= V_N(R_i,A_i,\beta_{\lambda i},\theta_i) \\ &+ V_C(R_i,A_i,\beta_{\lambda i},\theta_i)+V_\ell(R_i,A_i,\beta_{\lambda i},\theta_i). \end{aligned} \quad (2)$$

In Eq.(2), the attractive nuclear potential is represented by V_N among the two interacting nuclei and is calculated using a generalized theorem for proximity forces, given by Blocki and collaborators in 1977, called Prox77 [54]. The nuclear potential $V_N(R,A_i,\beta_{\lambda i},\theta_i)$ reads as [54−58]

$$V_N(R,A_i,\beta_{\lambda i},\theta_i)=4\pi\bar{R}\gamma b\Phi(s_0), \quad (3)$$

where 'b' is the surface diffuseness parameter and has a constant value of 0.99 fm.

The mean curvature radius ($\bar{R}$) is evaluated in terms of the radius vector of curvatures R_{i1} and R_{i2} for projectile and target nuclei, respectively, as follows:

$$\frac{1}{\bar{R}^2} = \frac{1}{R_{11}R_{12}} + \frac{1}{R_{21}R_{22}} + \frac{1}{R_{11}R_{22}} + \frac{1}{R_{21}R_{12}}. \tag{4}$$

The principal radii of curvature (R_{i1} and R_{i2}) for deformed-deformed or spherical-deformed cases is given [56] as

$$R_{i1}(\alpha_i) = \frac{\left[R_i^2(\alpha_i) + R_i'^2(\alpha_i)\right]^{3/2}}{R_i^2(\alpha_i) + 2R_i'^2(\alpha_i) - R_i(\alpha_i)R_i''(\alpha_i)}, \tag{5}$$

$$R_{i2}(\alpha_i) = \frac{R_i(\alpha_i)\sin\alpha_i}{\cos(\pi/2 - \alpha_i - \delta_i)} \quad (i = 1, 2). \tag{6}$$

For the spherical projectiles, Eq. (5) is simplified as $R_{11}(\alpha_1) = R_{12}(\alpha_1) = R_1(\alpha_1)$. In Eq. (3), the surface energy constant (γ) is expressed in terms of the asymmetry of nucleons as

$$\gamma = 0.9517\left[1 - 1.7826\left(\frac{N-Z}{A}\right)^2\right] \quad \text{MeVfm}^{-2}. \tag{7}$$

The term $4\pi\bar{R}\gamma b$ in Eq. (3) takes care of the shape and geometry of the colliding nuclei. The universal function, which depends on the shortest distance parameter (s_0) between the colliding nuclei along the collision axis, is given as [55, 56]

$$\Phi(s_0) = \begin{cases} -\frac{1}{2}(s_0 - 2.54)^2 - 0.0852(s_0 - 2.54)^3, \\ \qquad\qquad s_0 \le 1.2511 \quad \text{fm} \\ -3.437\exp\left(-\frac{s_0}{0.75}\right), s_0 > 1.2511 \quad \text{fm}. \end{cases} \tag{8}$$

Here, s_0 denotes the shortest distance between the two interacting nuclei [56], which is defined as

$$s_0 = R - X_1 - X_2, \tag{9}$$

where 'R' represents the distance between the interacting nuclei and X_1, X_2 are the projections of the P-T nuclei w.r.t. the colliding axis. These projections are determined as

$$\begin{aligned} X_1 &= R_1(\alpha_1)\cos(\theta_1 - \alpha_1); \\ X_2 &= R_2(\alpha_2)\cos(180 + \theta_2 - \alpha_2). \end{aligned} \tag{10}$$

Applying the minimization conditions on s_0 yields

$$\begin{aligned} \tan(\theta_1 - \alpha_1) = \tan(\delta_1) &= -\frac{R_1'(\alpha_1)}{R_1(\alpha_1)}, \\ \tan(180 + \theta_2 - \alpha_2) = \tan(\delta_2) &= -\frac{R_2'(\alpha_2)}{R_2(\alpha_2)}. \end{aligned} \tag{11}$$

The repulsive Coulomb potential (V_C) in Eq. (2) is defined for deformed-deformed colliding nuclei as follows [59, 60]:

$$\begin{aligned} V_C(R) = \frac{Z_1Z_2e^2}{R} + Z_1Z_2e^2 \sum_{\lambda=2,3,4,6}^{i=1,2} \left(\frac{R_i^\lambda(\alpha_i)}{R^{\lambda+1}}\right)\beta_\lambda Y_\lambda^{(0)}(\theta_i) \\ \times\left[\frac{3}{2\lambda+1} + \left(\frac{12}{7(2\lambda+1)}\right)\beta_\lambda Y_\lambda^{(0)}(\theta_i)\right]. \end{aligned} \tag{12}$$

The centrifugal potential in Eq. (2) is the rotational kinetic energy. This potential is dependent on the angular momentum ℓ and is expressed as follows [61, 62]:

$$V_\ell(R, A_i, \beta_{\lambda i}, \theta_i) = \frac{\hbar^2\ell(\ell+1)}{2I}; \quad I = \mu R^2. \tag{13}$$

Eqs. (2)–(13), which define the total interaction potential, provide significant insights into the characteristics of the interacting nuclei, which encompass barrier characteristics, including the barrier height V_B, barrier position R_B, and barrier curvature $\hbar\omega_B$. These parameters are affected by the degrees of freedom related to deformation and orientation, as indicated in the radius vector presented in Eq. (1). As a result, these parameters play a crucial role in determining the capture cross-sections, which is calculated using the ℓ-Wong formula [48, 49] for different combinations of the interacting P-T. This concept is discussed in the next section.

C. Capture cross-sections

The capture cross-section for deformed and oriented nuclei, interacting at the center of mass energies ($E_{\text{c.m.}}$), is evaluated using the Wong formula [59, 63], which is expressed as

$$\sigma_{\text{cap}} = \frac{R_B^2\hbar\omega_B}{2E_{\text{c.m.}}}\ln\left[1 + \exp\left(\frac{2\pi}{\hbar\omega_B}(E_{\text{c.m.}} - V_B)\right)\right], \tag{14}$$

and further transforms to the extended ℓ-summed Wong Model [48, 49]. This model incorporates the summation of the cross-section associated with each ℓ-partial wave, which can be mathematically represented as follows:

$$\sigma_{\rm cap}(E_{\rm c.m.},\theta_i)=\sum_{\ell=0}^{\ell_{\rm max}}\sigma_\ell=\frac{\pi}{k^2}\sum_{\ell=0}^{\ell_{\rm max}}(2\ell+1)P_\ell, \quad (15)$$

where $k=\sqrt{\frac{2\mu E_{\rm c.m.}}{\hbar^2}}$ and μ represents the reduced mass. The sharp cut-off approximation [55, 64] is employed to determine the maximum angular momentum, denoted as $\ell_{\rm max}$. Here, the barrier penetration or tunneling probability P_ℓ for each angular momentum (ℓ) is derived using the Hill-Wheeler approximation [65]:

$$P_\ell^{HW}(E_{\rm c.m})=\left[1+\exp\left(\frac{2\pi[V_B^\ell(E_{\rm c.m.})-E_{\rm c.m.}]}{\hbar\omega_B^\ell(E_{\rm c.m.})}\right)\right]^{-1}, \quad (16)$$

where $V_B^\ell(E_{\rm c.m.})$, $R_B^\ell(E_{\rm c.m.})$, and $\hbar\omega_B^\ell(E_{\rm c.m.})$ are obtained from the total interaction potential between the two interacting nuclei as determined in Eq. (2).

In addition, the integrated or average capture cross-sections are obtained by integrating over the range of orientations θ_i of the deformed nuclei having β_2,β_4,β_6 deformations [47], which is represented as

$$\sigma_{\rm int}(E_{\rm c.m.})=\int_{\theta_1=0}^{\pi/2}\int_{\theta_2=0}^{\pi/2}\sigma(E_{\rm c.m.},\theta_i)\sin\theta_1\sin\theta_2{\rm d}\theta_1{\rm d}\theta_2. \quad (17)$$

III. RESULT AND DISCUSSION

In the present work, we aim to explore the influence of modifications in the nuclear shape due to the incorporation of hexacontatetrapole deformation (β_6) along with (β_2), (β_4) deformed target nuclei. This study systematically investigates the collective influence of the magnitude and sign (±) of these higher-order deformations (up to β_6) on barrier characteristics of heavy-ion induced fusion reactions. Further, the elongated and compact configurations obtained from these modified barrier characteristics corresponding to β_4 and β_6 deformations are used to calculate the capture cross-sections ($\sigma_{\rm cap}$). The results are compared with available experimental data for center of mass energies $E_{\rm c.m.}$ spread across the Coulomb barrier. The analysis takes into account both spherical+deformed and deformed+deformed P-T combinations. This comprehensive study offers new insights into the influence of higher-order deformations up to the order of hexacontatetrapole deformation (β_6) on the fusion reaction dynamics. This section presents and discusses the findings of this study.

A. Nuclear Shape of hexacontatetrapole (β_6) deformed nuclei

Typically, the nuclear shape deviates from perfect spherical symmetry. These deviations arise from dipole moments linked to the neutron-to-proton ratio within the nuclei, which leads to a deformed nuclear shape. These nuclear deformations (β_λ) associated with the multipole order *i.e.,* $\lambda=2,3,4,6$ provide quadrupole, octupole, hexadexapole and hexacontatetrapole deformed nuclei shapes, respectively. The influence of these higher-order deformations is included in the nuclear shape via the radial vector, as defined in Eq. (1). To visualize the influence of β_6 deformation on the nuclear shape, we considered ^{246}Es nuclei subject to a significant magnitude of β_2, which is referenced from the data table provided by Möller *et al.* [50], while deformations β_4 = ± 0.05 and β_6= ±0.1 are assumed to analyze the significant effect of β_6, as shown in Fig. 1. The figure illustrates the evolution of the nuclear shape of ^{246}Es under various orders of deformations. The figure clearly illustrates the evolution of prolate-deformed nuclei with the incorporation of $\beta_4^\pm$ and $\beta_6^\pm$ deformations associated with the nuclei. The incorporation of β_4^+ with β_2^+ causes elongation, whereas the inclusion of β_4^- with β_2^+ causes the contraction of the prolate deformed nuclei. While Fig. 1(a) illustrates the modification in nuclear shape after the inclusion of $\beta_6^\pm$ in $\beta_2^+\beta_4^+$ deformed nuclei, Fig. 1(b) represents similar modifications in the shape of $\beta_2^+\beta_4^-$ deformed nuclei due to the incorporation of $\beta_6^\pm$. The figure shows that the incorporation of $\beta_6^\pm$ deformation introduces complexity to both the elongated shape of $\beta_2^+\beta_4^+$ deformed nuclei and the compressed shape of $\beta_2^+\beta_4^-$ deformed nuclei. Specifically, the presence of β_6^+ in both $\beta_4^\pm$ further elongates the nuclear shape along its poles and causes slight compression along the belly region of the nuclei. This elongation due to β_6^+ is more pronounced in the $\beta_2^+\beta_4^+$ case than the $\beta_2^+\beta_4^-$ deformed nuclei. On the other hand, β_6^- leads to compression on the poles and elongation along the belly, when incorporated in both β_4^+ and β_4^-. This flatness is more prominent at the poles for $\beta_2^+\beta_4^-$ deformed nuclei than $\beta_2^+\beta_4^+$, as shown in Fig. 1.

In other words, the incorporation of β_6^+ leads to elongation at the pole region and compression at the belly region, whereas β_6^- leads to the elongation at the belly region and compression at the poles. In addition to the sign (±) of the hexacontatertapole deformation, the extent of the elongation and compression in the deformed nuclear shape is also influenced by the magnitudes of the deformation associated with the nuclei. These observations highlight the sensitivity of nuclear shapes to the magnitude and signs of higher-order deformations, specifically β_6 in conjunction with β_2 and β_4 deformations. These modifications due to the collective influence of $\beta_2\beta_4\beta_6$ deformations significantly modify the nuclear barrier characteristics that govern the heavy-ion fusion dynamics. The next section discusses the effect of these deformed nuclear shapes on the barrier characteristics relative to the angle of orientations of the deformed nuclei with respect to the collision axis.

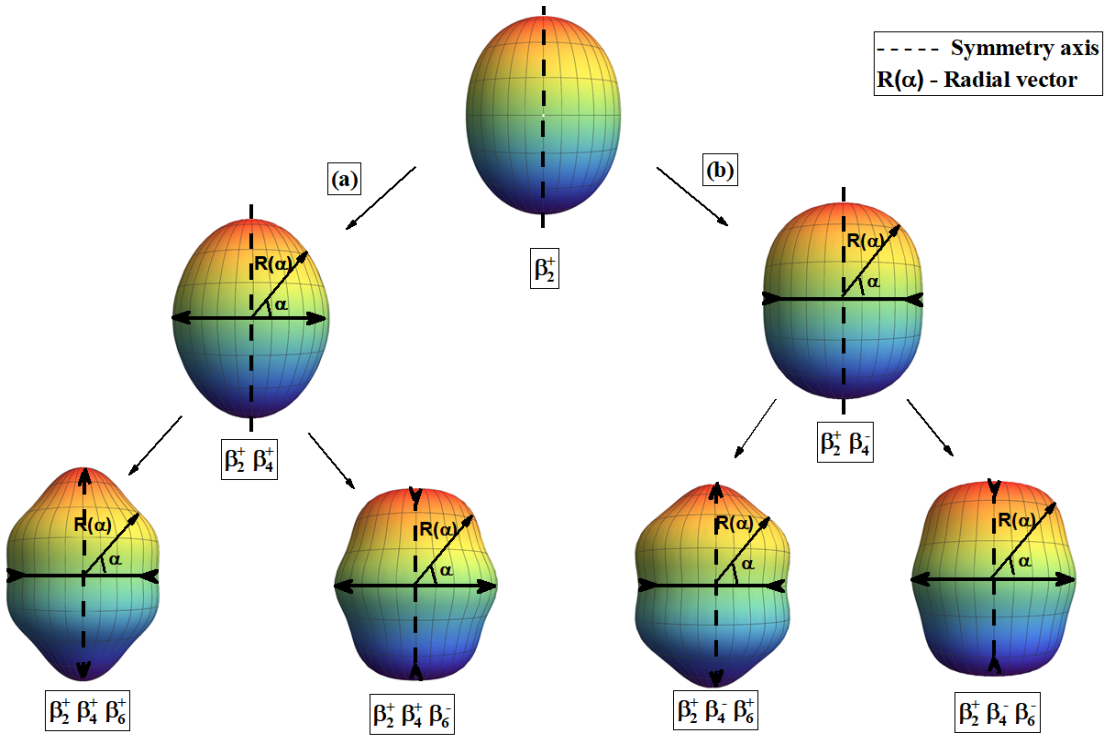

Fig. 1. (color online) Schematic diagram showing the shape evolution of the nucleus ^{246}Es incorporating the quadrupole (β_2), hexadecapole ($\beta_4^{\pm}$), and hexacontatetrapole ($\beta_6^{\pm}$); with β_2=0.248, considering $\beta_4 = \pm 0.05$ and $\beta_6 = \pm 0.1$.

B. Analysis of barrier characteristics of the hexadecapole (β_4) and hexacontatetrapole (β_6) deformed actinide targets

In the previous section, we discussed the influence of the magnitude and sign of $\beta_6^{\pm}$ on the shape of the nuclei along with the β_2^+ and $\beta_4^{\pm}$ deformations. This section aims to broaden the analysis by investigating the comprehensive effect of the modified shape of $\beta_4^{\pm}$ and $\beta_6^{\pm}$ deformed nuclei on the barrier characteristics, *i.e.*, barrier height (V_B) and barrier position (R_B) of the interacting nuclei. The objective of this analysis is to determine how $\beta_4^{\pm}$ and $\beta_6^{\pm}$ deformations modify the barrier characteristics when compared to a prolate deformed (β_2^+) case. For this analysis, we investigated the barrier characteristics for the ^{48}Ca-induced reactions with deformed actinide nuclei having non-zero values of β_2, β_4, and β_6 deformations. The variations in V_B and R_B with respect to target orientation (θ_2) ranging from 0° to 180° for different combinations of β_2, β_4, and β_6 deformations are illustrated in Fig. 2 and Fig. 3, respectively. These figures are divided into two panels, where panel (I) represents the barrier characteristics of $\beta_2^+\beta_4^+\beta_6^{\pm}$ deformed nuclei and panel (II) represents the barrier characteristics of $\beta_2^+\beta_4^-\beta_6^{\pm}$ deformed nuclei. Each panel of the analyzed actinide nuclei is classified into three distinct groups based on the values of β_4 and β_6 deformations. In particular, Fig. 2(a, b, g, and h) illustrates the scenarios in which the magnitude of β_4 is greater than β_6, while Fig. 2(c, d, i and j) depicts the cases in which the magnitude of β_4 is approximately equal to magnitude of β_6 deformation. Additionally, Fig. 2(e, f, k and l) showcases the instances in which the magnitude of β_6 deformation exceeds the magnitude of β_4 deformation. To conduct a thorough analysis of both the sign and magnitude of the associated β_6 deformation, both positive and negative β_6 deformations of equal magnitude were considered.

These figures show that the introduction of β_4^+ in quadrupole deformed nuclei lowers the barrier height V_B. Conversely, the incorporation of β_4^- in β_2 deformed nuclei increases V_B. The relative variation in V_B is influenced by the magnitudes of the β_2 and β_4 deformation parameters. A noticeable change in the orientation angle of the compact and elongated configurations has been observed alongside the barrier characteristics [36]. Further, the incorporation of $\beta_6^{\pm}$ in conjunction with β_2 and β_4 deformation modifies the shape of the nuclei at both the pole and belly positions, which causes variation in the barrier characteristics V_B and R_B. For instance, the addition of β_6^+ to $\beta_2^+\beta_4^{\pm}$ deformed nuclei lowers the barrier height V_B specifically at the target orientation θ_2=0° or 180°. Meanwhile, β_6^- increases the barrier height, as it compresses the shape of the nuclei around the poles at θ_2=0° or 180°. The impact of β_6 deformations is more pronounced for the orientations in the range of 0°−40° across all cases. However, as θ_2 surpasses this range, the value of V_B corresponding to $\beta_2\beta_4\beta_6$ deformed nuclei

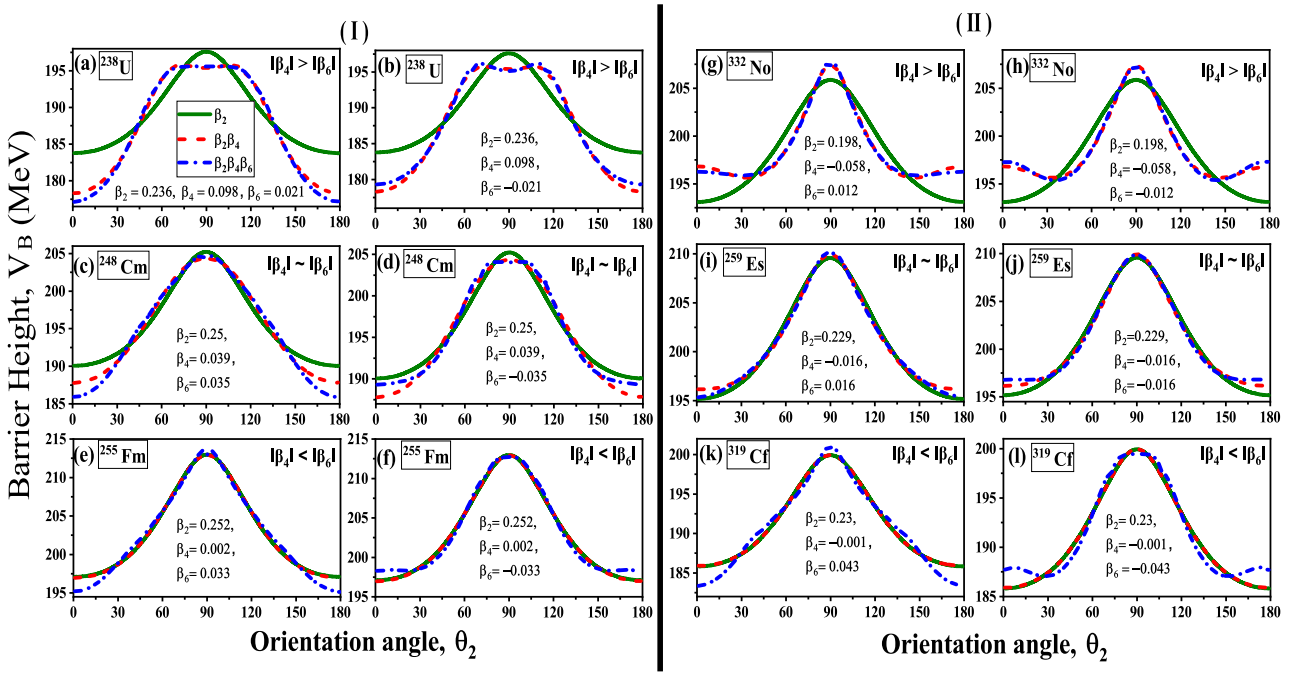

Fig. 2. (color online) A schematic representation illustrating the changes in barrier height (V_B) in relation to the orientation angle (θ_2) of deformed actinide nuclei. Panel (I) features nuclei with configurations $\beta_2^+\beta_4^+\beta_6^\pm$, while Panel (II) showcases $\beta_2^+\beta_4^-\beta_6^\pm$ deformed nuclei.

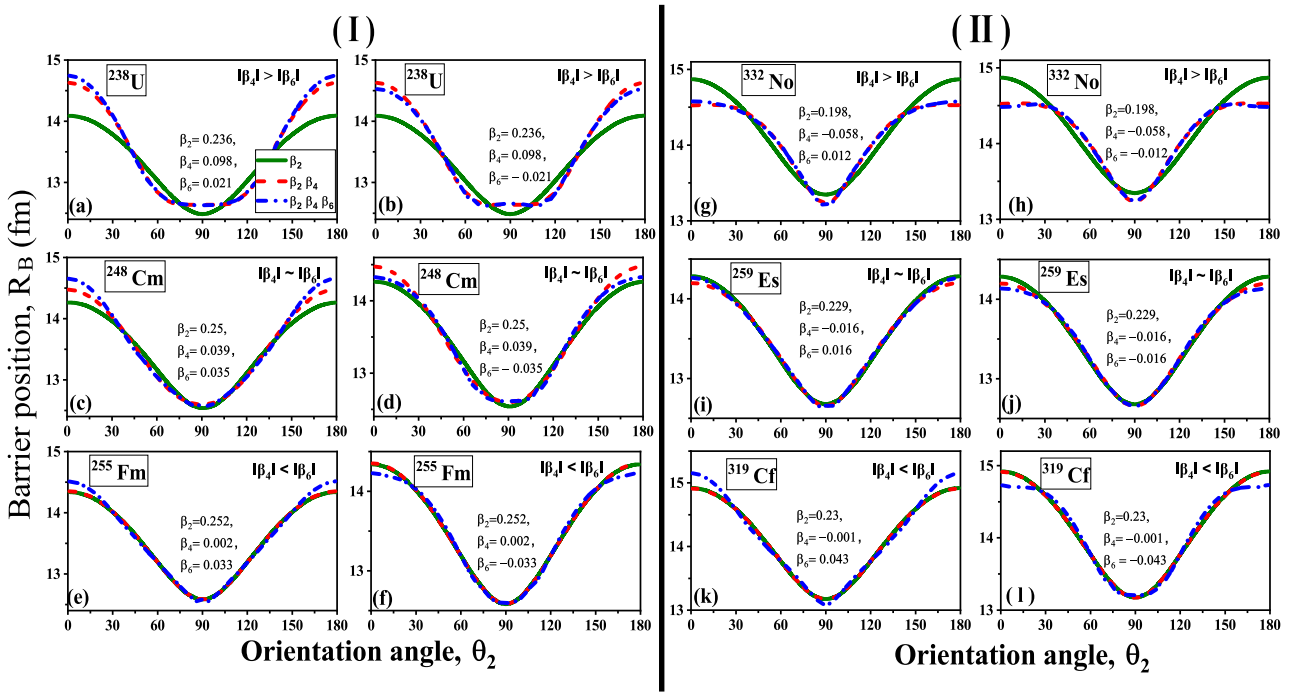

Fig. 3. (color online) A schematic representation illustrating the changes in barrier position (R_B) in relation to the orientation angle (θ_2) of deformed actinide nuclei. Panel (I) features nuclei with configurations $\beta_2^+\beta_4^+\beta_6^\pm$, while Panel (II) showcases $\beta_2^+\beta_4^-\beta_6^\pm$ deformed nuclei.

changes slightly as compared to $\beta_2\beta_4$ deformed nuclei. Conversely, an interesting variation can be observed at the target orientation $\theta_2 = 90°$, wherein the barrier height V_B increases for the case of β_6^+, while V_B decreases for the case of β_6^- relative to β_4. This variation, as discussed in the previous section, is linked to the compression and elongation of the nuclear shape at the belly of the nuclei due to the incorporation of β_6^+ and β_6^- deformations, respectively. It is important to note that the variation in V_B is not very significant at 90° for all cases. Additionally, in

scenarios where the value of β_4 is greater than β_6 and β_4 is approximately equal to β_6, the changes in barrier characteristics resulting from the inclusion of β_6 correspond to the deformation trend of β_4. Conversely, for cases in which β_4 is less than β_6, as illustrated in Fig. 2(e,f,k,l), the substantial impact of β_6 is evident because its magnitude is significantly larger than β_4. In a similar manner, an inverse variation with respect to V_B is observed in the analysis of barrier position R_B for all considered reactions. The variation in R_B for the considered reactions w.r.t orientation angle (θ_2) is shown in Fig. 3.

The incorporation of β_6 causes a significant shift in the optimum orientation in addition to variations in the barrier characteristics. These modified optimum orientations of the compact or elongated configuration of the β_6 deformed nuclei can significantly affect the overall dynamics of the nuclear interaction. These configurations are characterized by the maximal and minimum values of barrier height (V_B) and barrier position (R_B). The elongated configuration corresponds to the configuration with the minimum V_B and maximum R_B, whereas the compact configuration is associated with the configuration corresponding to the maximum V_B and minimum R_B. The analysis of the barrier height corresponding to β_2,β_4,β_6 in relation to the orientation angle (θ_2) is shown in Fig. 2. The figure clearly demonstrates that the variation in the barrier height V_B due to the incorporation of β_6 deformation in comparison to the β_4 deformation is significantly more pronounced in the orientation range θ_2=0° to 40° than those at θ_2=70° to 90°. The orientation range θ_2=0° to 40° represents the region with the minimum barrier height or the elongated configuration, while the orientation range θ_2=70° to 90° represents the region with the maximum barrier height or the compact configuration for the $\beta_2\beta_4\beta_6$ deformation combinations, respectively. Based on these results, additional emphasis will be placed on evaluating the impact of β_6 on the barrier characteristics at orientation angles ranging from 0° to 40°.

Thus far, we have established that the addition of β_6 deformation along with β_2 and β_4 provides noticeable alterations in the barrier characteristics for orientation angles ranging from 0° to 40°. To further explore the influence of the magnitude of β_6, we studied the variation in V_B for the previously mentioned range of orientation angle by varying the magnitude of β_6 deformation from -0.05 to 0.05, as demonstrated in Fig. 4. For the analysis, we consider the actinide nuclei having a significant magnitude of β_4 deformation as compared to the magnitude of β_6 (*e.g.* ^{244}Pu), and the nuclei with a smaller magnitude of β_4 deformation as compared to the magnitude of β_6 (*e.g.* ^{255}Fm). The study assumes both positive and negative signs for the magnitude of β_4 of the same nuclei. The results in Fig. 4 show that an increase in the magnitude of β_6^{+} significantly elongates the nucleus along its poles, thereby leading to a decrease in barrier height with respect to $\beta_4^{\pm}$ at θ_2= 0° or 180°. Conversely, an increase in

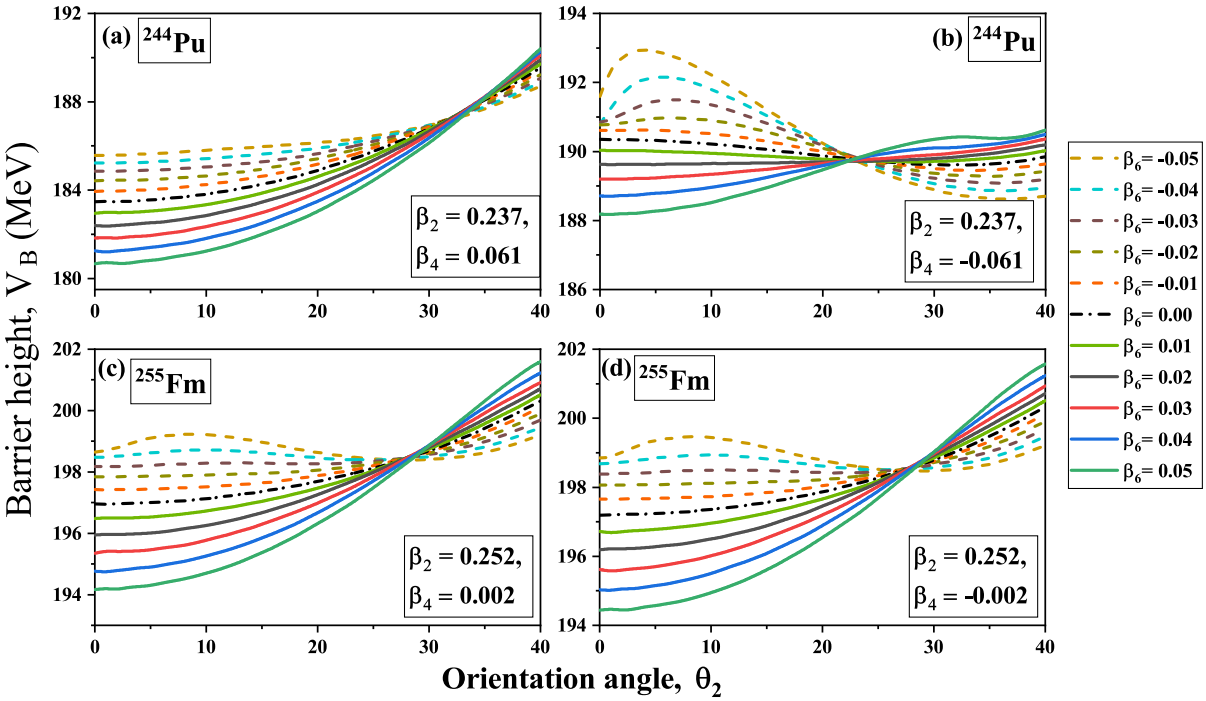

Fig. 4. (color online) Schematic diagram showing the variation of barrier height with respect to the orientation angle of the target varying from 0°–40° for values of β_6 ranging from –0.05 to +0.05 for nucleus with significant $\beta_4^{\pm}$ (^{244}Pu) and nucleus with a small magnitude of $\beta_4^{\pm}$ (^{255}Fm).

the magnitude of β_6^- causes an increase in the barrier height, which is due to an enhanced compression effect along the poles. Moving towards the target orientation θ_2=30°, variations in barrier height V_B can be observed for both β_6^+ and β_6^- cases. Increasing the positive value of β_6^+ yields a high value of V_B, while increasing the negative value of β_6^- results in a lower value of V_B at 30° or above, compared to $\beta_2\beta_4$ deformed nuclei. These variations are due to shape modifications that are caused by the incorporation of $\beta_6^\pm$. In Fig. 4(a) ^{244}Pu has a significant magnitude of β_4^+, and the elongated shape always appears at the orientation angle θ_2 = 0° regardless of the magnitude of $\beta_6^\pm$. However, in Fig. 4(b), a large negative value of β_4^- causes compression in the nuclear shape, and the orientation angle for the elongated configuration shifts to approximately $\theta_2 = 30°$. The addition of β_6^+ reduces this compression and brings back elongation at the poles $\theta_2 = 0°$ with increasing values. On the other hand, β_6^- further increases the compression at the poles, thus reinforcing the minimum barrier height at approximately $\theta_2 = 30°$.

On the other hand, for a smaller magnitude of $\beta_4^\pm$, the shape of the nuclei is mainly influenced by the magnitude and sign of the β_6 deformation. For instance, for both cases of β_6, the elongated configuration is observed at θ_2 =0° or 180°, as illustrated in Fig. 4(c, d). However, this orientation angle for the elongation configuration shift towards $\theta_2 \approx 30°$ for higher magnitudes of β_6^-. This analysis indicates that the magnitude and sign of the β_6 deformation have a significant influence on the barrier height V_B at the elongated configuration and also can shift the elongated configuration from 0° to approximately 30°, in conjunction with the influence of $\beta_2^+\beta_4^\pm$ deformations.

In order to conduct an in-depth analysis of the variation in barrier height V_B at the elongated configuration, we examined different sign combinations of quadrupole (β_2), hexadecapole (β_4), and hexacontatetrapole (β_6) deformations. This investigation focuses on several actinide nuclei to provide a comprehensive analysis of magnitudes and signs of deformations. The considered nuclei are examined by comparing the magnitudes of β_4 and β_6 deformation, which are categorized into three sets: (a) $\beta_4 > \beta_6$, (b) $\beta_4 \approx \beta_6$, and (c) $\beta_4 < \beta_6$. These three sets are analyzed for the deformation combinations of $\beta_2^+\beta_4^+\beta_6^+$, $\beta_2^+\beta_4^+\beta_6^-$, $\beta_2^+\beta_4^-\beta_6^+$, and $\beta_2^+\beta_4^-\beta_6^-$, as presented in Fig. 5. The deformations of the considered nuclei are taken from the data table provided in Möller *et al.* [50], and both positive and negative signs of β_4 and β_6 are considered. The figure reveals that for the combinations $\beta_2^+\beta_4^+\beta_6^+$ and $\beta_2^+\beta_4^+\beta_6^-$, the incorporation of β_6^+ results in a reduction of the barrier height (V_B), whereas the incorporation of β_6^- counteracts the influence of β_4^+, thus resulting in an increase in V_B when added to the deformed nuclei of $\beta_2^+\beta_4^+$. This result is consistent across all sets of magnitudes of β_4 and β_6, as depicted in Fig. 5. The same trend of variation in barrier height is obtained for β_6^+ and β_6^- when incorporated in the $\beta_2^+\beta_4^-$ deformed nuclei. These effects of β_6^+ and β_6^- are consistent when incorporated with $\beta_2^+\beta_4^-$ deformation combination for the cases in which $\beta_4 \approx \beta_6$ and $\beta_4 < \beta_6$, where the magnitude of β_4 is not significant, as illustrated in Fig. 5(b, c). However, a minor deviation in this trend occurs when $\beta_4 > \beta_6$, as shown in Fig. 5(a). Contrary to expectations, the addition of β_6^+ and β_6^- does not yield the anticipated decrease and increase in V_B when combined with β_4^-. This result seems to indicate that the predominance of β_4 over β_6 induces a structural modification. Further explicit analysis is necessary to quantify the interactions among these deformation parameters in the case of $\beta_4 > \beta_6$ and to assess their collective

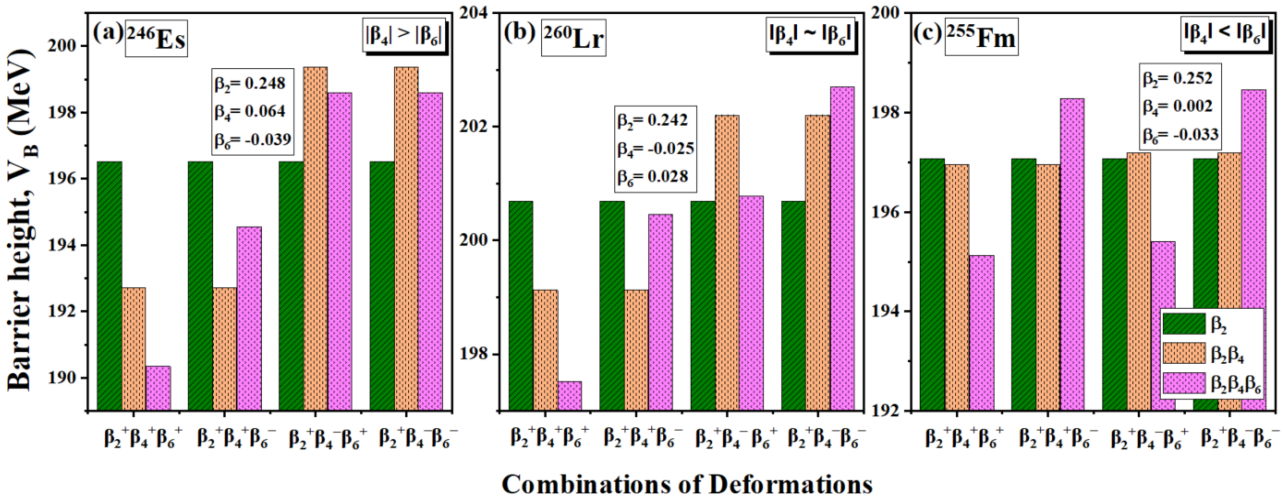

Fig. 5. (color online) Schematic diagram comparing the barrier heights of nuclei at elongated configuration corresponding to different combinations of deformations $\beta_2^+\beta_4^+\beta_6^+$, $\beta_2^+\beta_4^+\beta_6^-$, $\beta_2^+\beta_4^-\beta_6^+$, and $\beta_2^+\beta_4^-\beta_6^-$ for the considered nuclei having variation of magnitudes such as (a) $\beta_4 > \beta_6$, (b) $\beta_4 \approx \beta_6$, (c) $\beta_4 < \beta_6$.

impact on the barrier characteristics, specifically at the elongation configuration.

To further examine the influence of the $\beta_6^{\pm}$ deformation in the presence of a substantial β_4^- deformation, we analyzed the variations in V_B at elongated configurations for several nuclei illustrated in Fig. 6. In this context, we refer to Fig. 4(b), which demonstrates that the magnitude of β_4^- is significant than the magnitude of $\beta_6^{\pm}$ and the presence of β_4^- deformation contributes to the overall shape of the nuclei. As previously mentioned, an increase in the magnitude of β_6^+ is associated with a decrease in V_B and results in elongation at an angle of 0°. However, for lower magnitudes of β_6^+, both compression and elongation effects arise due to β_4^- and β_6^+, respectively, creating a balance in the shape, which results in a higher V_B than that produced solely by β_4^-. On the other hand, the β_6^- deformation intensifies the compression at the poles but continues the elongation near $\theta_2 \approx 30°$, thus resulting in a decrease in V_B as its magnitude increases. The relevant evidence for this behavior in the nuclei is depicted in Fig. 6(c,d). Meanwhile, as the magnitudes of both β_6^+ and β_6^- deformations increase, the values of V_B become comparable. This behavior is illustrated in Fig. 6(a, b), which shows the comparable and lower values of V_B for $\beta_6^{\pm}$ in relation to β_4^-. Nevertheless, the relative change in V_B for $\beta_6^{\pm}$ compared to β_4^- is not significant.

The previous discussion highlighted impactful results on the role of hexacontatetrapole deformations in heavy-ion induced reactions for a spherical projectile (^{48}Ca) with β_6 deformed target actinide nuclei. Next, we aim to analyze the influence of the projectile orientation (θ_1) on barrier characteristics for deformed-deformed P-T combinations. To this end, the variations in the barrier height V_B with respect to the orientation angle of both the deformed target and projectile nuclei are systematically analyzed using color-mapped contour plots for cases in which the reactions having minimum and significant magnitude of projectile deformation, as shown in Fig. 7. The first case is shown in Fig. 7(a) for the reaction of ^{48}Ti (β_2 = 0.011) +^{238}U (β_2 = 0.236, β_4 = 0.098, β_6 = -0.021), in which the magnitude of β_2 deformation of the projectile is smaller and thus the barrier height V_B is less sensitive to the projectile orientation and there is no significant change in the orientation angles for the compact and elongated configurations. While the compact configuration with the highest barrier height occurs at $\theta_1 = 97°, \theta_2 = 110°$, the elongated configuration with the lowest barrier is observed at $\theta_1 = 1°, \theta_2 = 0°$. These configurations are dependent on the target orientation, *i.e.*, a change in the projectile orientation for such a P-T combination would not impose any significant change in the barrier height for both configurations. Meanwhile, for the reaction of ^{54}Cr (β_2 = 0.161, β_4 = 0.048, β_6 = -0.024) +^{248}Cm (β_2 = 0.250, β_4 = 0.039, β_6 = -0.035), where both P-T have significant deformations, the barrier height V_B is sensitive to the orientation angle of both projectile and target nuclei, as shown in Fig. 7(b). While the compact configuration with the highest V_B is observed at θ_1, θ_2 =

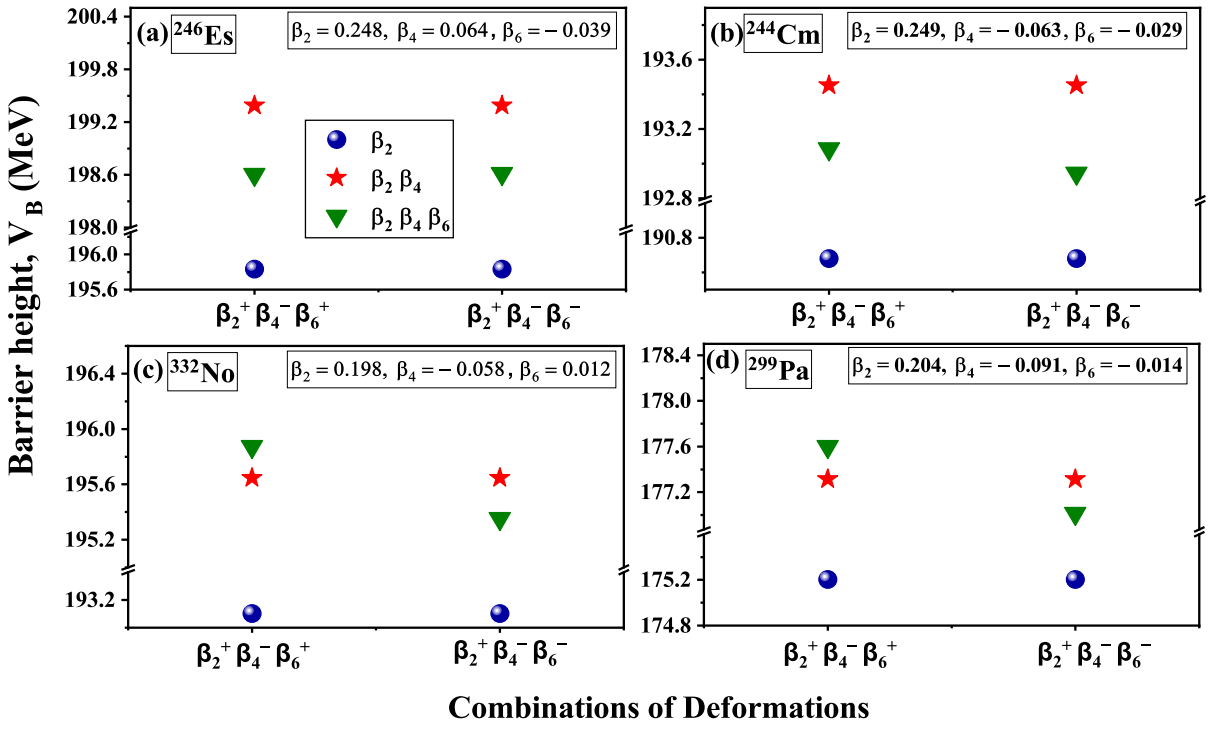

Fig. 6. (color online) Schematic diagram comparing the barrier heights of different actinides with ^{48}Ca projectile at the elongated configuration for the $\beta_2^+\beta_4^-\beta_6^+$, and $\beta_2^+\beta_4^-\beta_6^-$ combination of deformations in the case of $\beta_4 > \beta_6$.

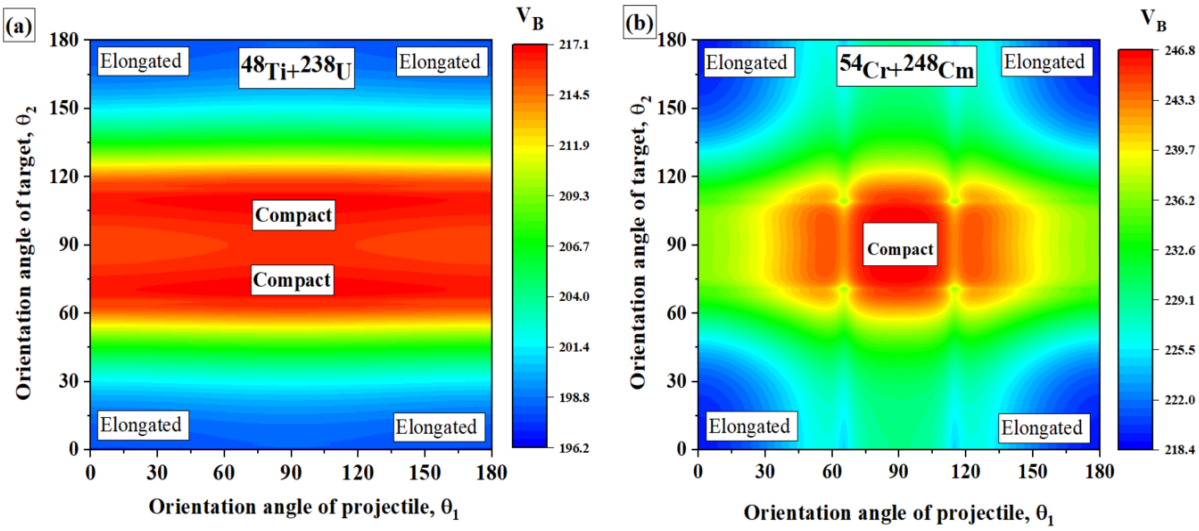

Fig. 7. (color online) Schematic representation of the variation in interaction barrier height as a function of the projectile (θ_1) and target (θ_2) orientation angles for deformed–deformed P-T combinations: (a) ^{48}Ti+^{238}U, and (b) ^{54}Cr+^{248}Cm.

90°, 101°, the elongated configuration with the lowest V_B occurs at $\theta_1, \theta_2 = 180°, 0°$. For this P-T combination, a slight change in the projectile orientation θ_1 can impose a significant change in the barrier height V_B, which signifies the influence of projectile orientation θ_1 along with the target orientation θ_2. These findings underline the possible influence of the projectile deformation on the barrier characteristics of deformed-deformed P-T combinations.

The previous sections discussed the influence of $\beta_2\beta_4\beta_6$ deformations on the barrier characteristics of spherical+deformed and deformed+deformed P-T nuclei, along with their modified compact and elongated configurations. To further examine the role of these configurations on the fusion dynamics of the considered P-T combinations, we study the total interaction potential V_T ($= V_C + V_N$) as a function of the separation distance R for the reaction ^{48}Ti + ^{238}U, shown in Fig. 8. The total interaction potential V_T directly reflects the effect of nuclear deformations and orientations introduced through both the Coulomb potential V_C and nuclear potential V_N. It is worth noting that both the projectile, ^{48}Ti, and the target, ^{238}U, are prolate deformed. Fig. 8 demonstrates the variations in V_T for the elongated and compact configurations of the deformed projectile and target (P-T) in comparison to the spherical scenario. Fig. 8(a) shows the variations for a spherical projectile nucleus, while Fig. 8(b) includes the deformation of both the projectile and target nuclei. In both cases, the elongated configuration lowers the barrier height V_B compared to the compact and spherical configurations (P-T are spherical), thereby reducing the extra push energy required for fusion. This lowering of the barrier is more pronounced when projectile deformation is taken into account, as seen in Fig. 8(b). These results are attributed to the modification in the shape of the nuclei as a result of the addition of the deformations. Consequently, the inclusion of higher-order deformations for both projectile and target nuclei leads to a lowering of the fusion barrier and enhances the probability of fusion at elongated configurations.

So far, we have systematically analyzed the impact of both the magnitude and sign (±) of symmetric higher-order deformations (up to β_6) on barrier characteristics, *i.e.*, barrier height (V_B) and barrier position (R_B), for both spherical+deformed and deformed+deformed P-T combinations. In the next section, we discuss our implementation of these modified barrier characteristics and their corresponding compact and elongated configurations to determine the capture cross-sections $\sigma_{\rm cap}$, which reflect the combined influence of hexacontatetrapole deformations $\beta_6^{\pm}$ over a wide range of incident energies $E_{\rm c.m.}$ spanning across the Coulomb barrier.

C. Capture cross-sections for spherical + deformed and deformed+deformed projectile-target

In this section, the relevance of the obtained modified barrier characteristics and their corresponding compact and elongated configurations for both spherical+deformed and deformed+deformed projectile–target (P–T) combinations is exercised to calculate the capture cross-sections. The capture cross-sections ($\sigma_{\rm cap}$) are obtained using the ℓ-summed Wong model for the center of mass energies $E_{\rm c.m.}$ lying across the Coulomb barrier. Initially, the $\sigma_{\rm cap}$ for the P-T combination ^{48}Ca + ^{244}Pu is calculated using β_4 and β_6 deformed nuclei at their respective elongated and compact configurations in comparison to the available experimental data [51], as shown in Fig. 9. This figure illustrates the variation in $\sigma_{\rm cap}$ for the reaction under consideration at their optimum as well as integrated orientations across various values of $E_{\rm c.m.}$. The

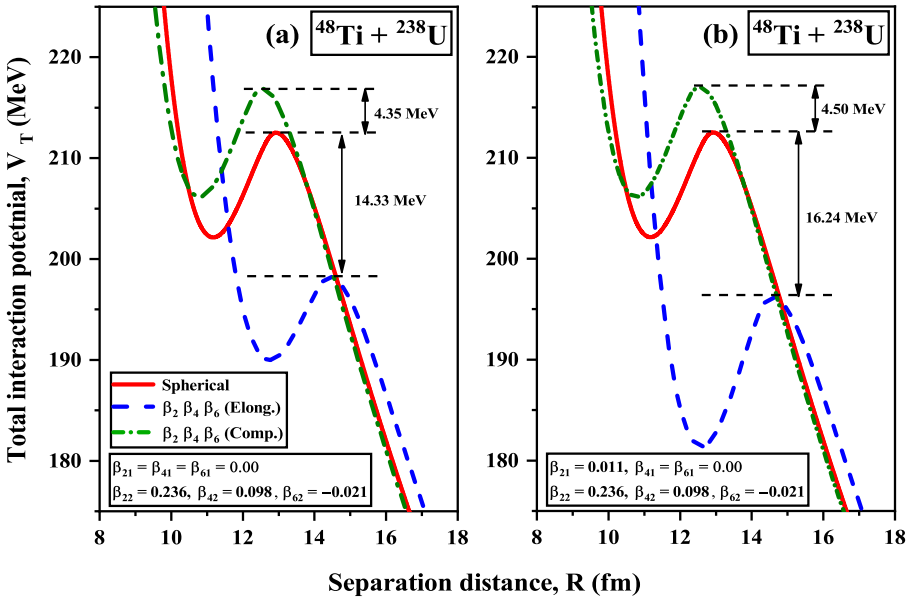

Fig. 8. (color online) Total interaction potential V_T (MeV) as a function of separation distance R (fm) for the P-T combination of (a) ^{48}Ti ($\beta_{21}=\beta_{41}=\beta_{61}=0.00$) + ^{238}U ($\beta_{22}=0.236,\beta_{42}=0.098,\beta_{62}=-0.021$) and (b) ^{48}Ti ($\beta_{21}=0.011,\beta_{41}=\beta_{61}=0.00$) + ^{238}U ($\beta_{22}=0.236,\beta_{42}=0.098,\beta_{62}=-0.021$). The variations in V_T and R are illustrated for both elongated and compact configurations of the deformed nuclei, along with the case in which both projectile and target are considered spherical (red line).

figure shows that the elongated configuration yields an enhanced value of $\sigma_{\rm cap}$ compared to that of the compact configuration for both $\beta_2\beta_4$ and $\beta_2\beta_4\beta_6$ deformations. This difference is attributed to the lower V_B for capture at the elongated configuration, which is associated with the shape modifications induced by these deformations. Additionally, the calculated integrated cross-sections reflect the average effect of the cross-sections obtained at various orientations, which lie between the compact and elongated configurations. As the elongated configuration yields better agreement with experimental data, $\sigma_{\rm cap}$ is calculated at the elongated configuration for all considered P-T combinations involving ^{48}Ca induced reactions with ^{238}U and ^{248}Cm, as well as ^{36}S and ^{48}Ti induced reactions with ^{238}U. The obtained $\sigma_{\rm cap}$ values corresponding to both the elongated and integrated configurations of $\beta_2\beta_4$ and $\beta_2\beta_4\beta_6$ deformations are compared with available experimental data, as shown in Fig. 10. However, the center of mass energies of the reactions depicted in Fig. 10(a, d) lie above the barrier, beyond the V_B corresponding to the elongated configuration for both β_4 and β_6 deformations; thus, the cross-sections calculated at elongated configurations align well with the experimental cross-sections. For the reaction involving ^{48}Ca+^{238}U, the presence of β_6^- in ^{238}U hinders $\sigma_{\rm cap}$ for energies $E_{\rm c.m}$ lying below and near the Coulomb barrier, which is caused by an increase in V_B in comparison to the case for β_4^+ , as shown in Fig. 10(b). Meanwhile, the presence of the deformed projectile ^{36}S with β_6^+ deformation enhances the capture cross-sections compared to the case that only contains the β_4 deformation [Fig. 10(c)]. Furthermore, the

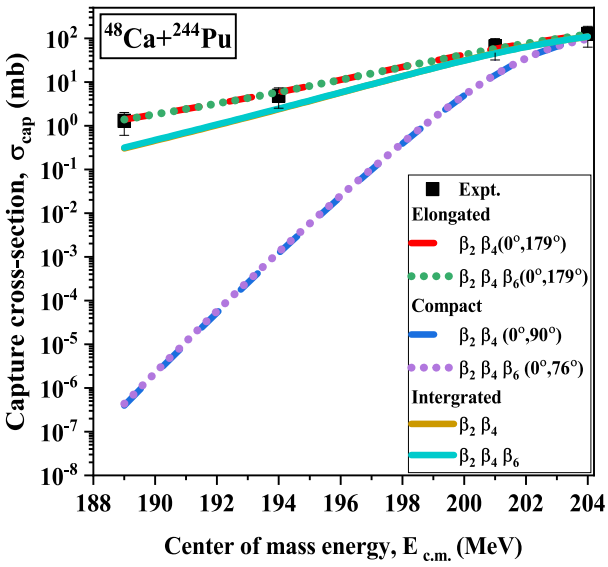

Fig. 9. (color online) Schematic diagram of Capture cross-sections ($\sigma_{\rm cap}$) calculated using ℓ-summed Wong model as a function of $E_{\rm c.m.}$ at compact and elongated configurations of $\beta_2\beta_4$ and $\beta_2\beta_4\beta_6$ along with the cross-sections integrated over all orientations for reaction ^{48}Ca+^{244}Pu.

integrated capture cross-sections hold significant value in light of experimental studies. However, the integrated cross-sections calculated for these considered reactions, which account for the averaged contributions from all P–T orientations, exhibit a suppression relative to those obtained for the elongated configurations, as shown in Fig. 10. To address this suppression and to determine the

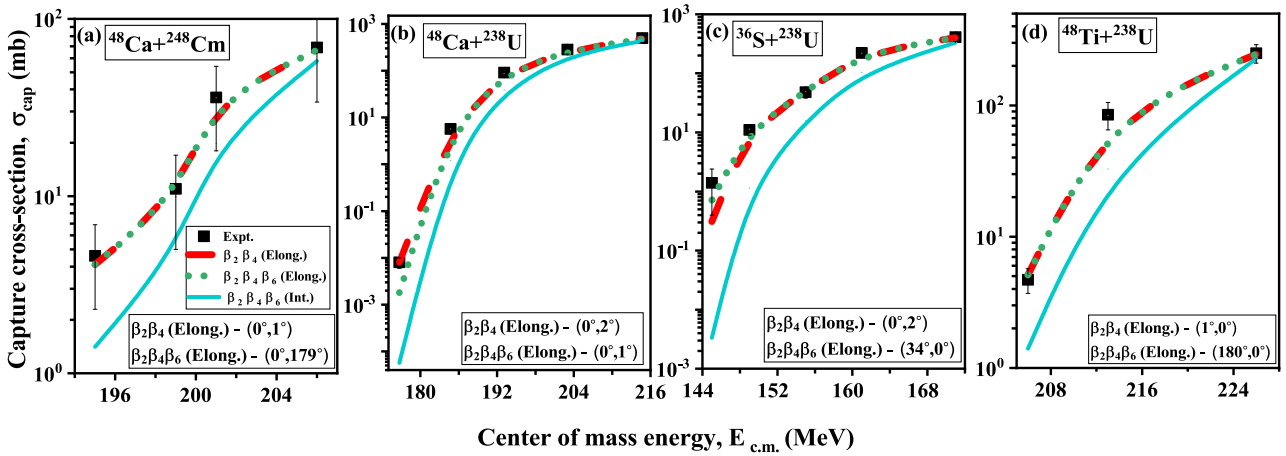

Fig. 10. (color online) Schematic diagram of capture cross-sections ($\sigma_{\rm cap}$) obtained using ℓ-summed Wong model as a function of $E_{\rm c.m.}$ at elongated configurations and integrated over all orientations of $\beta_2\beta_4$ and $\beta_2\beta_4\beta_6$ for considered P-T combinations and compared with available experimental data.

relevance of all orientations of $\beta_2\beta_4\beta_6$ through integrated cross-sections from an experimental perspective, we analyzed $\sigma_{\rm cap}$ using the Wong Model. The obtained results are compared with experimental cross-sections as well as values of $\sigma_{\rm cap}$, which were calculated at the elongated configuration using the ℓ-summed Wong Model for the reaction ^{48}Ca+^{238}U, as illustrated in Fig. 11. The analysis reveals that the integrated cross-sections derived from the Wong Model offer a decent agreement with experimental data when the deformation up to β_6 is incorporated, while the integrated cross-sections determined using the ℓ-summed Wong Model are notably suppressed as partial waves are included up to $\ell_{\rm max}$ only. Thus, we can conclude that the inclusion of β_6 alongside $\beta_2\beta_4$ can significantly affect $\sigma_{\rm cap}$ at both elongated and integrated orientations.

The considered reactions have experimental data available for energies lying above the barrier. To quantify the impact of $\beta_6^{\pm}$ relative to $\beta_4^{\pm}$, we evaluated the capture cross-sections for the reaction ^{48}Ca+^{246}Es forming the CN with Z=119 at centre-of-mass energies ($E_{\rm c.m.}$) ranging from 180 to 220 MeV, which spans across the barrier. These capture cross-sections are calculated using the Wong formula at the elongated configurations and integrated cross-sections of all orientations of P-T of $\beta_2\beta_4$ and $\beta_2\beta_4\beta_6$ with both positive and negative signs. As seen in

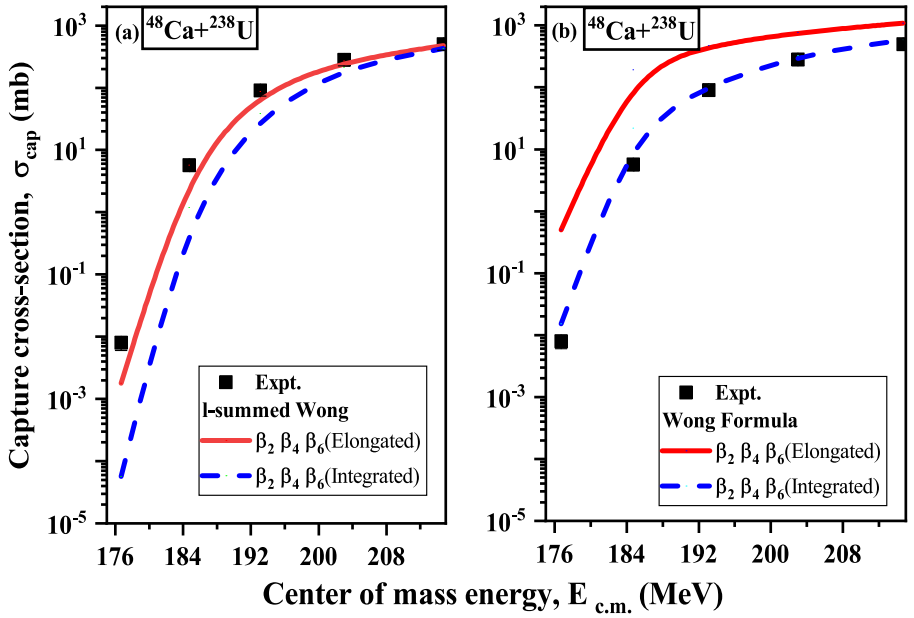

Fig. 11. (color online) Schematic representation of capture cross-sections ($\sigma_{\rm cap}$) calculated using (a) ℓ-summed Wong model and (b) Wong Model as a function of $E_{\rm c.m.}$. Results are shown for elongated configurations as well as integrated calculations for $\beta_2\beta_4\beta_6$ deformed case, and compared with the available experimental data for the considered P–T combination of ^{48}Ca+^{238}U.

Fig. 12(a), incorporating β_6^+ into $\beta_2^+\beta_4^+$ markedly enhances $\sigma_{\rm cap}$, whereas β_6^- introduces a noticeable suppression. Conversely, in Fig. 12(b), the value of $\sigma_{\rm cap}$ for the $\beta_2^+\beta_4^-$ deformation in the presence of $\beta_6^\pm$ is enhanced owing to variations in V_B , which is caused by the shape modification in the case of $\beta_2^+\beta_4^-\beta_6^\pm$, as discussed in the previous section. On the other hand, the integrated cross-sections follow a similar trend to the elongated configurations upon the inclusion of $\beta_2\beta_4^\pm\beta_6^\pm$ deformations; however, they show suppression comparatively to elongated configurations, as illustrated in Fig. 12 and discussed in the previous paragraph. Furthermore, according to the analysis presented in Refs. [11, 66], regarding the synthesis of superheavy nuclei (SHN) with Z = 120, the combination of ^{50}Ti and ^{249}Cf as the projectile and target is identified as the most favourable configuration for achieving SHN with Z = 120. Consequently, the estimated capture cross-sections are derived using Wong's formula, which incorporates higher-order deformations $\beta_2\beta_4$ and $\beta_2\beta_4\beta_6$ at their elongated and integrated cross-sections as a function of the range of center of mass energies that lie across the Coulomb barrier, as depicted in Fig. 12 (c). The figure shows that the addition of β_6^- in conjunction with β_2^+ and β_4^+ results in a reduction in the cross-sections in both configurations when compared to the scenario involving $\beta_2^+\beta_4^+$ alone. Nevertheless, this reduction is less significant in the integrated configuration owing to the collective effects across all orientations.

Furthermore, we comprehensively compared our calculated results with those derived from the microscopic Time-Dependent Hartree–Fock (TDHF) method. This comparison is illustrated in Fig. 13, which depicts the capture cross-sections ($\sigma_{\rm cap}$) calculated using the ℓ-summed Wong model and compares them with results acquired using the Density-Constrained Frozen Hartree–Fock (DC-FHF) potential within the TDHF framework [67], alongside experimental data from [68] available for the reaction ^{48}Ca + ^{238}U forming the compound nucleus ^{286}Cn. This recent TDHF-based study is particularly important, as it investigates the influence of higher-order deformations (β_2, β_4, β_6) and their orientation effects on the capture dynamics. Therefore, this work is chosen for comparison and analysis in our study. The results in Fig. 13 indicate that cross-sections obtained using the ℓ-summed Wong model for the elongated configuration are in closer agreement with the experimental data compared to the integrated cross-sections $\sigma_{\rm cap}$, as well as the integrated and elongated cross-sections obtained from the TDHF calculations.

Overall, these findings underscore the crucial role of higher-order β_6 deformations, alongside β_2 and β_4, in modifying barrier characteristics and capture cross-sections in heavy-ion reactions that lead to the formation of superheavy nuclei.

IV. SUMMARY

The present work offers a deep insight into the higher-order deformations (up to hexacontatetrapole deformations β_6) and their corresponding orientations on the synthesis of superheavy nuclei (SHN). The analysis highlights the explicit roles of different signs and magnitudes of β_6 on the heavy-ion induced reactions in conjunction with quadrupole (β_2) and hexadecapole (β_4) deformations of the target nuclei. We consider the P-T combinations ^{48}Ca+^{248}Cm, ^{48}Ca+^{244}Pu, ^{48}Ca+^{238}U, ^{36}S+^{238}U , and

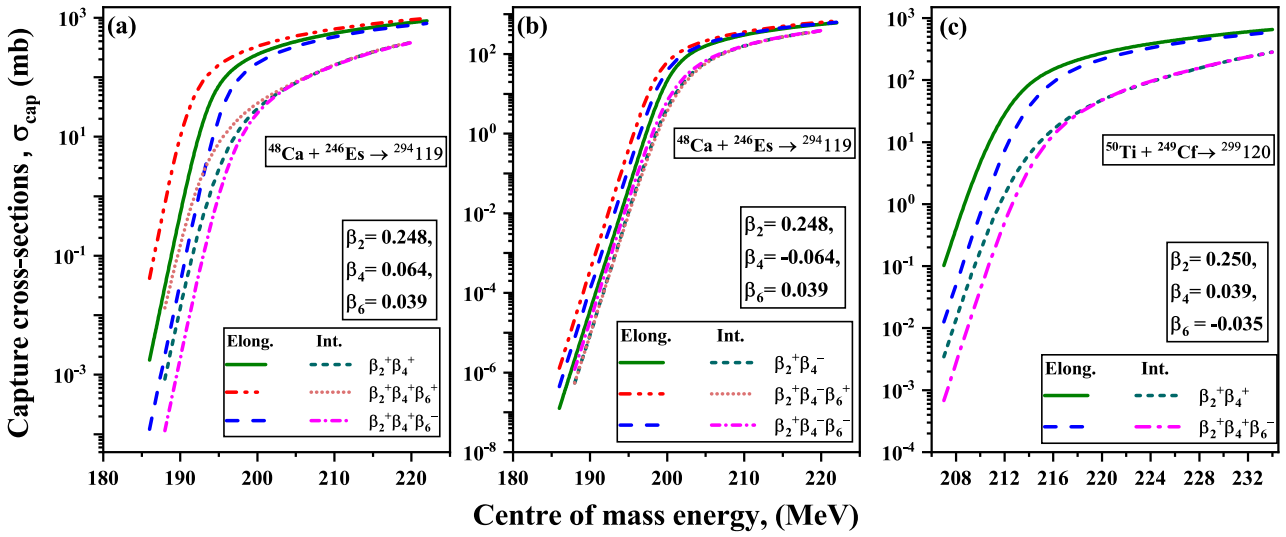

Fig. 12. (color online) Schematic diagram of capture cross-sections ($\sigma_{\rm cap}$) as a function of center-of-mass energy for the reaction (a) ^{48}Ca+^{246}Es (Z=119) with $\beta_2^+\beta_4^+$, $\beta_2^+\beta_4^+\beta_6^\pm$ combinations, (b) ^{48}Ca+^{246}Es (Z=119) with $\beta_2^+\beta_4^-$, $\beta_2^+\beta_4^-\beta_6^\pm$ combinations, (c) ^{50}Ti+^{249}Cf (Z=120) calculated using the Wong's formula. The results are shown for combinations of the deformations considered at their elongated configuration and integrated cross-section over all orientations.

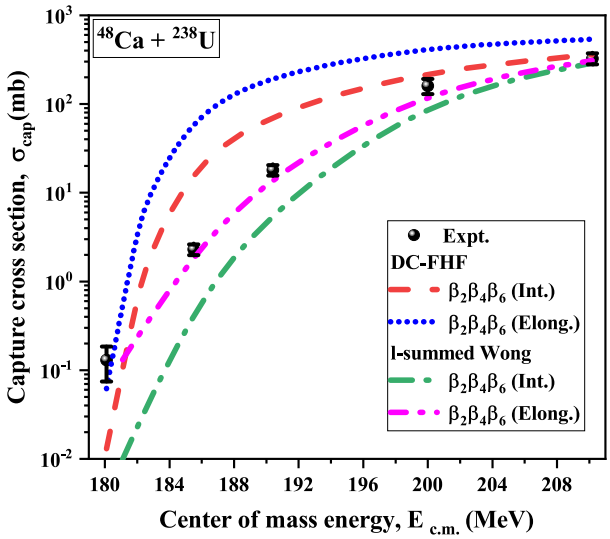

Fig. 13. (color online) Schematic representation of the capture cross-sections (σ_{cap}) obtained from the ℓ-summed Wong model as a function of the center-of-mass energy ($E_{c.m.}$) for the reaction ^{48}Ca+^{238}U evaluated at elongated configurations and integrated over all orientations for deformations $\beta_2\beta_4\beta_6$. The calculated results are compared with the corresponding experimental data and with σ_{cap} values extracted from the DC-FHF model at both configurations.

^{48}Ti+ ^{238}U leading to the formation of SHN ^{296}Lv, ^{292}Fl, ^{286}Cn, ^{274}Hs, and ^{286}Fl. The shape evolution of the deformed actinide target nuclei due to the incorporation of these deformations alters the barrier characteristics, *i.e*, the barrier height V_B and barrier position R_B , of the interactions that influence the formation of the SHN, where variations depend on the sign of $\beta_6^{\pm}$. For instance, the incorporation of β_6^{+} leads to simultaneous elongation along the poles and compression at the belly, whereas the incorporation of β_6^{-} leads to elongation at the belly and compression along the poles in the $\beta_2^{+}\beta_4^{\pm}$ deformed nuclei. The influence of β_6 is further analyzed for three magnitude relations: (a) $\beta_4 > \beta_6$, (b) $\beta_4 \approx \beta_6$, and (c) $\beta_4 < \beta_6$. The analysis indicates notable differences in the barrier characteristics for the elongated configuration, while no such differences are observed for the compact configuration, which shifts the focus towards the elongated configuration considering various combinations of β_2,β_4,β_6 deformations. The findings indicate that the incorporation of β_6^{+} deformation lowers V_B, whereas the incorporation of β_6^{-} increases V_B when integrated with $\beta_2^{+}\beta_4^{\pm}$ deformation for the cases in which $\beta_4 \approx \beta_6$ and $\beta_4 < \beta_6$. These results are in agreement with the previously defined behavior of $\beta_4^{\pm}$ deformed nuclei. However, for the cases with $\beta_4 > \beta_6$, deviations from this trend are observed in $\beta_2^{+}\beta_4^{-}\beta_6^{\pm}$ deformed nuclei owing to the predominance of β_4 over β_6. The possible influence of the orientation of the deformed projectile nuclei has also been discussed. These modified barrier characteristics are utilized to calculate the capture cross-sections for the considered P-T combinations. The results show better agreement with available experimental data at elongated configurations for the synthesis of SHN. While the above-mentioned results provide significant understanding of the reaction dynamics of the nuclei involving β_2, β_4, and β_6 deformations having an axially symmetric shape, future work will investigate the relevance of octupole (β_3) deformations where reflection asymmetry becomes significant.

References

[1] S. Hofmann, J. Nucl. Radiochem. Sci. **4**, R1 (2003)
[2] Y. Abe, Y. Aritomo, T. Wada *et al.*, J. Phys. G: Nucl. Part. Phys. **23**, 1275 (1997)
[3] V. L. Litnevsky, V. V. Pashkevich *et al.*, Phys. Rev. C **89**, 034626 (2014)
[4] C. Shen, G. Kosenko, and Y. Abe, Phys. Rev. C **66**, 061602 (2002)
[5] V. Volkov, G. Adamian, N. V. Antonenko *et al.*, Phys. Atom. Nuclei **64**, 1116 (2001)
[6] S. Chopra, Hemdeep, and R. K. Gupta, Phys. Rev. C **95**, 044603 (2017)
[7] Y. T. Oganessian and V. K. Utyonkov, Rep. Prog. Phys. **78**, 036301 (2015)
[8] C. Jiang, B. Back, K. Rehm *et al.*, Eur. Phys. J. A **57**, 235 (2021)
[9] O. R. Smits, C. E. Düllmann, P. Indelicato *et al.*, Nat. Rev. Phys. **6**, 86 (2024)
[10] G. Montagnoli and A. Stefanini, Eur. Phys. J. A **59**, 138 (2023)
[11] S. Rana, R. Kumar, and M. Bhuyan, Phys. Rev. C **104**, 024619 (2021)
[12] B. B. Back, H. Esbensen, C. L. Jiang *et al.*, Rev. Mod. Phys. **86**, 317 (2014)
[13] A. S. Umar, V. E. Oberacker *et al.*, Phys. Rev. C **81**, 064607 (2010)
[14] Z.-Q. Feng, G.-M. Jin, J.-Q. Li *et al.*, Nucl. Phys. A **816**, 33 (2009)
[15] W. Reisdorf and M. Schdel, Z. Physik A - Hadrons and Nuclei **343**, 47 (1992)
[16] M. Beckerman, Rep. Prog. Phys. **51**, 1047 (1988)
[17] S. Jain, M. K. Sharma, and R. Kumar, Chin. Phys. C **46**, 014102 (2022)
[18] S. Mitsuoka, H. Ikezoe, K. Nishio *et al.*, Phys. Rev. C **62**, 054603 (2000)
[19] V. A. B. Zagatto, C. E. Aguiar, J. Lubian *et al.*, Phys. Rev. C **111**, 024617 (2025)
[20] M. S. Gautam, Mod. Phys. Lett. A **30**, 1550013 (2015)
[21] M. Gautam, Indian J. Phys. **90**, 335 (2016)
[22] A. Nasirov, A. Fukushima *et al.*, Nucl. Phys. A **759**, 342 (2005)
[23] L. Zhu, Z.-Q. Feng, C. Li *et al.*, Phys. Rev. C **90**, 014612 (2014)
[24] M. Kaur, M. K. Sharma, and R. K. Gupta, Phys. Rev. C **86**, 064610 (2012)

[25] V. V. Sargsyan, G. G. Adamian *et al*., Phys. Rev. C **85**, 037602 (2012)
[26] G. Fazio, G. Giardina, A. Lamberto *et al*., Journal of the Physical Society of Japan **72**, 2509 (2003)
[27] K. Kim, Y. Kim, A. K. Nasirov *et al*., Phys. Rev. C **91**, 064608 (2015)
[28] R. A. Kuzyakin, V. V. Sargsyan, G. G. Adamian *et al*., Phys. Rev. C **92**, 014603 (2015)
[29] R. K. Gupta, M. Balasubramaniam, R. Kumar *et al*., J. Phys. G: Nucl. Part. Phys. **31**, 631 (2005)
[30] V. Y. Denisov and N. A. Pilipenko, Phys. Rev. C **76**, 014602 (2007)
[31] V. Y. Denisov and N. A. Pilipenko, Phys. Rev. C **81**, 025805 (2010)
[32] N. Jain, M. Bhuyan, and R. Kumar, Phys. Rev. C **109**, 034617 (2024)
[33] S. Rana, M. Bhuyan, R. Kumar *et al*., Phys. Rev. C **110**, 024601 (2024)
[34] H. Sharma, S. Jain, R. Kumar *et al*., Phys. Rev. C **108**, 044613 (2023)
[35] S. Jain, M. K. Sharma, and R. Kumar, Phys. Rev. C **101**, 051601 (2020)
[36] H. Sharma, S. Jain, R. Kumar *et al*., Eur. Phys. J. A , **59**, 71 (2023)
[37] M. Ismail, W. Seif, and M. Botros, Nucl. Phys. A **828**, 333 (2009)
[38] M. Manhas, R. K. Gupta, Q. F. Li *et al*., Phys. Rev. C **74**, 034603 (2006)
[39] D. L. Hendrie, B. G. Harvey, J. R. Meriwether *et al*., Phys. Rev. Lett. **30**, 571 (1973)
[40] J. M. Moss, Y. D. Terrien, R. M. Lombard *et al*., Phys. Rev. Lett. **26**, 1488 (1971)
[41] G. Pálla, H. Geramb, and C. Pegel, Nucl. Phys. A **403**, 134 (1983)
[42] C. R. Morton, A. C. Berriman *et al*., Phys. Rev. C **64**, 034604 (2001)
[43] T. Rumin, K. Hagino, and N. Takigawa, Phys. Rev. C **61**, 014605 (1999)
[44] A. Iwamoto, P. Möller, J. R. Nix *et al*., Nucl. Phys. A **596**, 329 (1996)
[45] V. E. Oberacker, M. Seiwert, and W. Greiner, Z. Phys. A **310**, 287 (1983)
[46] R. K. Gupta, M. Manhas, and W. Greiner, Phys. Rev. C **73**, 054307 (2006)
[47] D. Jain, R. Kumar, and M. K. Sharma, Nucl. Phys. A **915**, 106 (2013)
[48] R. Kumar, M. K. Sharma, and R. K. Gupta, Nucl. Phys. A **870-871**, 42 (2011)
[49] R. Kumar, Phys. Rev. C **84**, 044613 (2011)
[50] P. Möller, A. J. Sierk, T. Ichikawa *et al*., At. Data Nucl. Data Tables **109**, 1 (2016)
[51] G. Itkis, M. G. Knyazheva, I. Itkis *et al*., Eur. Phys. J. A **58**, 178 (2022)
[52] J. P. Davidson, Rev. Mod. Phys. **37**, 105 (1965)
[53] R. S. Mackintosh, Rep. Prog. Phys. **40**, 731 (1977)
[54] J. Błocki, J. Randrup, W. J. Świątecki *et al*., Ann. Phys. **105**, 427 (1977)
[55] R. Kumar, M. Bansal, S. K. Arun *et al*., Phys. Rev. C **80**, 034618 (2009)
[56] R. K. Gupta, N. Singh, and M. Manhas, Phys. Rev. C **70**, 034608 (2004)
[57] M. Seiwert, W. Greiner, V. Oberacker *et al*., Phys. Rev. C **29**, 477 (1984)
[58] N. Malhotra and R. K. Gupta, Phys. Rev. C **31**, 1179 (1985)
[59] C. Y. Wong, Phys. Rev. Lett. **31**, 766 (1973)
[60] Z. Gao-Long, L. Xiao-Yun, and L. Zu-Hua, Chin. Phys. Lett. **25**, 1247 (2008)
[61] R. Bass, Nucl. Phys. A **231**, 45 (1974)
[62] W. Swiatecki, Nucl. Phys. A **376**, 275 (1982)
[63] N. Wang, J. Chen, Y. Wang *et al*., Phys. Rev. C **111**, 024621 (2025)
[64] W. Scobel, H. H. Gutbrod, M. Blann *et al*., Phys. Rev. C **14**, 1808 (1976)
[65] D. L. Hill and J. A. Wheeler, Phys. Rev. **89**, 1102 (1953)
[66] H. Albers, J. Khuyagbaatar, D. Hinde *et al*., Phys. Lett. B **808**, 135626 (2020)
[67] X.-X. Sun and L. Guo, Phys. Rev. C **107**, 064609 (2023)
[68] K. Nishio, S. Mitsuoka, I. Nishinaka *et al*., Phys. Rev. C **86**, 034608 (2012)